Identification and Estimation of the Bandwidth of Different Acoustic Arrays Composed of Tonpilz Transducers in Engineering Sonar Systems

Naghmeh Sheida[1], Hamid M. Sedighi[1,2]*, Ali Valipour[1]

[1] Mechanical Engineering Department, Faculty of Engineering, Shahid Chamran University of Ahvaz, 61357-43337 Ahvaz, Iran

[2] Drilling Center of Excellence and Research Center, Shahid Chamran University of Ahvaz, 61357-43337 Ahvaz, Iran

* Correspondence: Hamid M. Sedighi (hmsedighi@gmail.com)

Abstract: Underwater electroacoustic transducers detect and localize targets beneath the water surface by generating acoustic waves. Due to their high power and simple structure, Tonpilz transducers are commonly used in underwater applications. To enhance data transmission speed and improve target detection capabilities using these transducers, it is necessary to increase their frequency bandwidth. One method of broadening the bandwidth is by adding damping elements to the transducer; however, this approach reduces the transmitted voltage response. In other words, increasing the frequency bandwidth comes at the cost of a reduced voltage output. To address this issue, arrays are typically used. Arrays are groups of transducers arranged together to improve performance and direct acoustic energy in a desired direction. Since accurate identification and estimation of bandwidth are critical to the performance and efficiency of a transducer—and ultimately the electroacoustic array—and given the high cost of manufacturing such transducers and arrays, the finite element method (FEM) is considered a highly desirable tool for analyzing and estimating the frequency bandwidth of electroacoustic arrays. Planar arrays are the simplest type of array. In the present study, the frequency responses of several planar arrays in square, circular, and diamond configurations have been comprehensively examined using finite element modeling. The effects of changes in array geometry, as well as variations in the number of transducers and their spacing, on the arrays' performance have been predicted. Based on the obtained results, among three kinds of square arrays with different inter-element spacing, the array with a spacing of 0.4λ between transducers exhibits the widest bandwidth. Additionally, among the two simulated circular arrays, the one with more elements demonstrates a higher transmitted voltage response and broader bandwidth. Furthermore, altering the array shape can reduce side lobes and help achieve the desired beam pattern. Overall, selecting the optimal array depends on the intended application, operating range, working environment, existing noise levels, and potential interference sources. Depending on these conditions, any of the examined arrays can be utilized effectively.

Keywords: Finite element method; Tonpilz transducer; Frequency response; Transmit voltage response; Ultrasonic arrays; COMSOL multiphysics

1 Introduction

Ultrasonic transducers are used to convert acoustic and electrical energies into one another. Studying these transducers and their applications requires knowledge in mechanics, electricity, magnetism, solid-state physics, and acoustics. In general, the applications of ultrasonic transducers can be categorized into two groups. In the first group, ultrasonic waves are used for transmitting and receiving information. In the second group, these waves are applied to materials to perform processes such as ultrasonic cleaning, welding of metallic and plastic materials, soldering, and machining. Ultrasonic transducers are used for transmitting and receiving information, and thus, they can be utilized in sonar systems. Sonar is the process of locating underwater targets using sound waves. Various mechanisms are employed in ultrasonic transducers to convert electrical and acoustic energies. Some of these methods utilize electric fields, while others employ magnetic fields. However, in most underwater transducers, piezoelectric properties are

used for this purpose. Piezoelectric transducers are widely used in the field of ultrasonics due to their small size, light weight, and high efficiency. In addition, they are relatively inexpensive, and due to the low electrical impedance of piezoelectric rings, they require lower voltages for excitation. A group of these transducers that vibrate in the longitudinal direction are known as Tonpilz transducers.

Tonpilz transducers, in their simplest form, consist of one or more pairs of piezoelectric rings placed between two metallic components. An electrode is positioned between each pair of piezoelectric elements. The adjacent piezoelectric rings in each pair are polarized in opposite directions, and voltage is applied to the electrode situated between the two rings. The components of the transducer are held together by a pre-stressed bolt, which applies a residual stress to maintain the assembly. Figure 1 illustrates a cross-sectional view of a Tonpilz transducer.
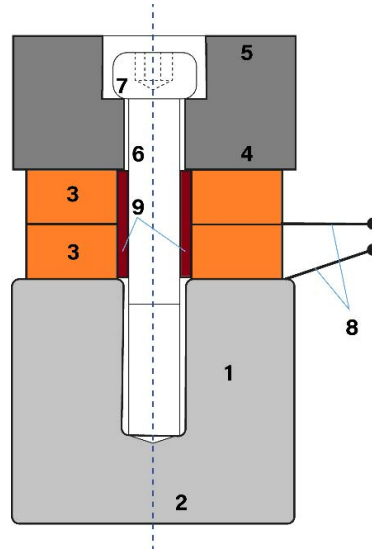
Figure 1. Sectional view of the Tonpilz transducer: (1,2) Head mass; (3) Piezoelectric rings; (4,5) Tail mass; (6,7) Bolts; (8) Electrodes; (9) Insulating tube

Arrays are typically designed such that the size of their constituent elements is small compared to the wavelength of sound in the propagation medium, allowing each element to be treated as a point source of wave emission [1]. This implies that arrays generally consist of a large number of transducers, making their fabrication a time-consuming and expensive process. Therefore, accurate modeling of these arrays is of great importance. Furthermore, to precisely analyze the behavior of the array, it is essential to consider the interaction between the array and its surrounding environment during the modeling process [2]. As a result, the finite element method is commonly used for modeling arrays.

The first sandwich transducer was built in 1917 by Paul Langevin, a prominent French physicist. Forty-two years later, in 1959, Harry B. Miller developed the first Tonpilz transducer to improve the performance of sandwich-type transducers. Today, Tonpilz transducers are among the most commonly used sonar projectors due to their simple structure, favorable performance, and low cost. In addition to sonar systems, these transducers are also employed in industries such as ultrasonic cleaning and the welding of metals and plastics [3].

Tonpilz transducers emit acoustic waves in a specific direction and can be implemented in ultrasonic arrays. These transducers possess high acoustic power, and when arranged compactly in an array, they can generate high-intensity sound waves with a large directivity index. Tonpilz transducers can be actuated using piezoelectric or magnetostrictive materials [4, 5]. The Tonpilz transducer used in this study comprises six piezoceramic rings vibrating along their thickness, a head mass, a tail mass, and a bolt. The operating frequency of Tonpilz transducers can range from 1 to 50 kHz. This frequency is essentially their resonance frequency. Although resonance and the resulting large displacements are typically avoided in many industrial applications, in sonar and underwater acoustic systems, resonance is desirable because the acoustic waves emitted by a transducer vibrating at its resonance frequency yield the highest sound pressure levels.

Piezoelectric materials are a class of smart, polar, and anisotropic materials that couple mechanical and electrical properties. When mechanical stress is applied to these materials, electrical charges appear on their surfaces and an electric field is generated—this phenomenon is known as the direct piezoelectric effect. Furthermore, when a voltage is applied, these materials undergo strain proportional to the magnitude and direction of the resulting electric field; this is referred to as the indirect piezoelectric effect [6, 7]. Piezoelectric materials can function as actuators to induce motion in objects. They are also used in the structure of ultrasonic Tonpilz transducers. In these devices, piezoceramic rings vibrate longitudinally, aligned with their polarization direction. The simplest and earliest methods for modeling

ultrasonic transducers are one-dimensional approaches. These methods assume that the radial dimensions of the transducer are much smaller than its longitudinal dimensions, allowing radial vibrations to be neglected [3, 8]. One such one-dimensional approach is the equivalent circuit method. The earliest of these is the BVD (Butterworth Van-Dyke) model. In this model, the input electrical impedance of a piezoelectric ring near its resonance frequency is represented by an RLC circuit in parallel with a capacitor. The elements of this circuit are frequency-independent and are derived from the material's elastic, piezoelectric, and dielectric constants [3]. Ballato [9] have thoroughly explained the advantages and limitations of this model. The equivalent circuit of a piezoelectric ring is shown in Figure 2.

The most important and widely used equivalent circuit model for piezoelectric rings and discs was introduced by Mason in 1948 [3]. In Mason's method, a piezoelectric ring is modeled as a network with two mechanical ports and one electrical port. Mason's model for a piezoelectric ring is shown in Figure 3.
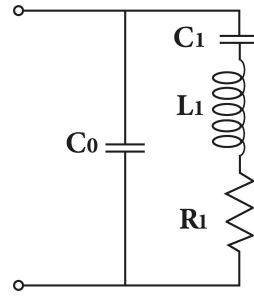
Figure 2. The BVD model for a piezoelectric ring near its resonance frequency
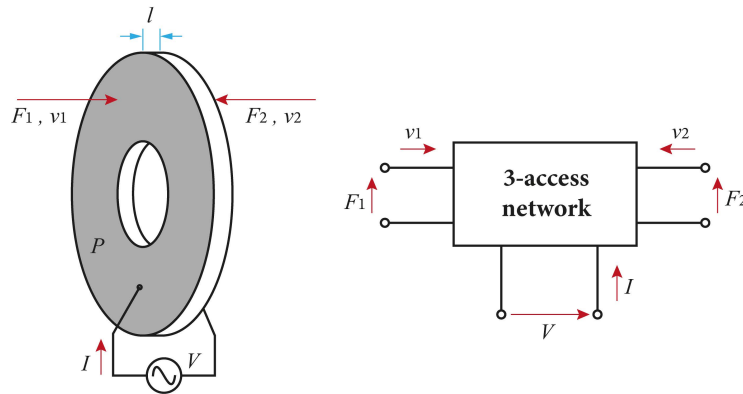
Figure 3. The Mason equivalent circuit model for a piezoelectric ring

In Figure 3, vi and Fi, respectively, represent the velocities of the annular surfaces of the piezoelectric rings and the forces applied to these surfaces. V and I denote the voltage applied to the electrodes and the current passing through them. The equations governing this network are derived from the fundamental equations of piezoelectric materials.

Another one-dimensional modeling approach is the model developed by Iula et al. [10]. Unlike the previously mentioned one-dimensional models, this method neglects longitudinal vibrations and instead calculates the radial vibration modes of thin piezoelectric rings using a one-dimensional matrix-based model. In the Iula model, the assumed rings are stress-free on their annular surfaces but sustain stress on their lateral surfaces. Each ring is represented as a two-port mechanical and one-port electrical network.

Iula's model and other one-dimensional models were not suitable for analyzing rings with comparable longitudinal and radial dimensions. Therefore, researchers have proposed models to examine the behavior of piezoelectric rings in two or three dimensions. For instance, Iula et al. [11] later used a three-dimensional matrix model to study the behavior of solid piezoelectric cylinders. In this model, the vibrations of the piezoelectric component in the longitudinal and radial directions are described using two coupled differential equations. The solution to these equations consists of two orthogonal wave functions. Using Iula's three-dimensional model, the first radial and longitudinal vibration modes can be calculated with sufficient accuracy, and the relationships between the applied voltage on the cylinder and the velocities and forces on its surfaces for these modes can be determined. Since these two primary modes are of greatest importance in ultrasonic transducer applications, this model provides adequate precision for the design and optimization of such transducers. Following Iula's model, Mancic and Radmanovic [12] developed a more comprehensive model to study the three-dimensional vibrations of piezoelectric rings. Jalili and Goudarzi [13] also

proposed a three-dimensional model for analyzing hollow piezoceramic cylinders using the principles of electricity and an equivalent admittance matrix.

In this paper, Mancic's matrix model is used for the analytical solution of the Tonpilz transducer. The model for a piezoelectric ring is illustrated in Figure 4. In this model, radial vibration modes are not neglected, and the mutual effects of different modes as well as the influence of the surrounding medium on the acoustic power of the transducer are included in the analysis. The equations for these components are similar to those of piezoelectric rings, with the difference that piezoelectric constants are omitted, and the metallic components, unlike the piezoelectric rings, are isotropic [14]. By setting the inner diameter of the rings to zero, the frequency response of a disc or solid cylinder geometry can also be obtained [3]. Finally, by connecting the mechanical and electrical ports of the piezoelectric rings, metallic components, and bolt in a series-parallel configuration, a complete transducer is modeled.
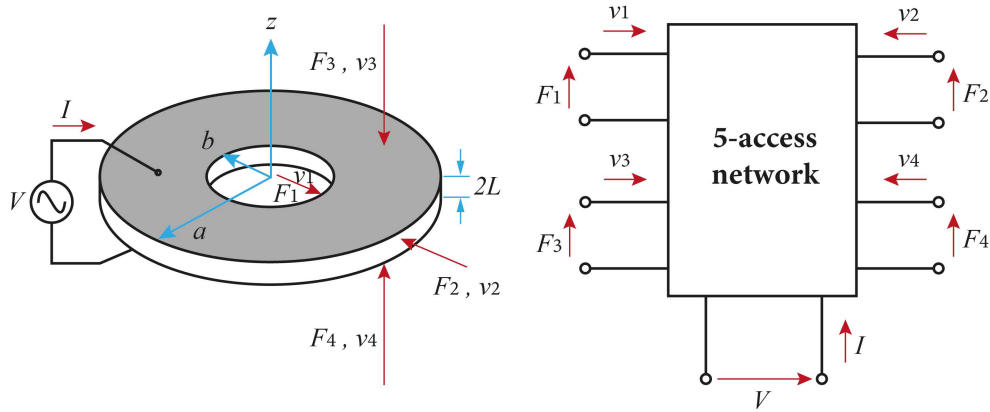
Figure 4. Mancic model for a piezoelectric ring

Finite element analysis of ultrasonic transducers can be performed using software such as ANSYS and COMSOL. Kim and Roh [15] proposed a new structure for the Tonpilz transducer to reduce the quality factor and increase its bandwidth by decreasing the head mass through the creation of a hole. After optimizing the transducer structure using a genetic algorithm and regression analysis, they examined the impact of this mass reduction on the transducer's performance using ANSYS software. Harikrishnan et al. [16] also compared the directivity of spherical and cylindrical hydrophones with polyurethane coatings using COMSOL software. In their study, they analyzed the effect of the shape—spherical or cylindrical—of the polyurethane coating on the directivity as well.

Recent advancements in Tonpilz transducer technology have dramatically improved their performance for underwater operations, specifically with regard to bandwidth improvement, material structural optimization, and acoustic production. One of the excellent new designs proposed by Gou et al. [17] involved the use of impedance-matching networks combined with modified head mass geometries to gain an additional 6 dB of transmitter voltage response and 3.5 times the active power output, while extending the frequency range by a factor of 1.5. Another example was achieved by Ji et al. [18] with new drive-stack configurations, and specifically the creation of well-designed non-uniform piezoceramic stack configurations made from disks of various thicknesses produced improved flexural vibrational modes and an ability to provide a 24.8% bandwidth gain over traditional uniform stack designs.

Another example of advancement in the development of high-power and wideband multimode Tonpilz transducers was investigated by Hadeed et al. [19] whereby the optimization of the head mass radius and modifications in geometry provided advancement with low-frequency broadband performance. A number of experimental investigations were conducted with stack configurations paving way greater degree of insight on achieving ultra-wideband performance with optimization in layer design and coupling [20]. Use of multi-objective optimization algorithms were also explored by Karami and Morsali [21] to best design performance criteria across bandwidth, output pressure, and stability. Furthermore, design and calibration of Tonpilz transducer was presented Pigatto et al. [22] to efficiently identify the optimized frequency in medical applications. Structural optimization methods, coupled with dynamic analysis which has provided the ability to modify transducer components for specific acoustic output and mechanical strength presented by Chen et al. [23]. These improvements show a clear trend toward efficient, wideband, and applicati on specific Tonpilz transducers for new and imaginative underwater acoustic systems.

In this paper, a systematic approach for designing Tonpilz transducers is presented. First, a Tonpilz transducer is designed using analytical and numerical methods, and its characteristics and performance are analyzed. Then, the results obtained from these methods are compared together to examine the best performance and efficiency. Since the primary aim of this paper is to present a design methodology for Tonpilz transducers, simplifications have been applied throughout the modeling process wherever possible—provided that the essential and key characteristics of the transducer are preserved.

2 Theoretical Framework

As mentioned earlier, the one-dimensional methods are not suitable for calculating the first radial vibration mode of a transducer and are typically used for modeling transducers whose longitudinal dimensions are significantly larger than their radial dimensions. When the longitudinal and radial dimensions of a transducer are of the same order of magnitude, the resonance frequency of the radial modes approaches that of the thickness mode. Therefore, more comprehensive two- or three-dimensional models must be employed for accurate analysis [24]. Accordingly, in this study, the approximate three-dimensional matrix model developed by Mancic is used to determine the resonance frequency. This model is easier to implement, and since it accounts for the interaction between the transducer's vibration modes, the analysis results derived from it can be reliably used for precise transducer design.

2.1 Mancic's Matrix Model for a Piezoceramic Ring

Due to the influence of the radial modes of the ring on the transducer's modes, it is essential to model the piezoceramic ring in three dimensions [11, 12]. In Mancic's model, the ring is treated as a three-dimensional structure with axial symmetry and is analyzed in a polar coordinate system, taking into account the effects of the surrounding medium on all of its surfaces. The greatest challenge in accounting for the mutual influence of different vibration modes in piezoceramic rings is the accurate solution of the partial wave differential equations that describe the vibrations of piezoceramic elements. Therefore, approximate methods are typically used to solve them.

Due to the influence of the radial modes of the ring on the transducer's modes, it is essential to model the piezoceramic ring in three dimensions [11, 12]. In Mancic's model, the ring is treated as a three-dimensional structure with axial symmetry and is analyzed in a polar coordinate system, taking into account the effects of the surrounding medium on all of its surfaces. The greatest challenge in accounting for the mutual influence of different vibration modes in piezoceramic rings is the accurate solution of the partial wave differential equations that describe the vibrations of piezoceramic elements. Therefore, approximate methods are typically used to solve them.

In Mancic's model, the solution to these equations consists of two o1rthogonal wave functions, each of which is a function of time and the coordinate axis along which the wave propagates. The mechanical and electrical boundary conditions for these functions are expressed in the form of approximate integrals. Consequently, the effect of the surrounding environment on the ring is approximately modeled [3]. In Mancic's model, the piezoceramic ring shown in Figure 4 is polarized along its thickness direction. The assumed coordinate system is aligned such that the z-axis corresponds with the polarization direction. The origin of the coordinate system is placed at the center of the ring. The outer radius of the ring is denoted as a, the inner radius as b, and its thickness as 2h. Two electrodes are placed on the annular surfaces of the ring, and an alternating voltage is applied across these electrodes. v_i, Z_i, and F_i, respectively, represent the velocity of each surface of the ring (P_i), the acoustic impedance, and the forces applied to these surfaces.

In piezoceramic rings, due to the presence of electrodes on the annular surfaces, the E_θ and E_r components of the electric field vector on these surfaces are zero and are also assumed to be zero within the ring. Furthermore, due to axial symmetry, none of the variables depend on the angular coordinate θ, and the displacement u_θ is considered zero. The displacements $u_r = u_r(r,t)$ and $u_z = u_z(z,t)$ represent the ring's deformation in the radial and axial directions, respectively. Under these assumptions, the fundamental equations for a piezoceramic ring in polar coordinates are expressed as [3]:

$$
\begin{aligned}
T_{rr} &= c_{11}^D S_{rr} + c_{12}^D S_{\theta\theta} + c_{13}^D S_{zz} - h_{31} D_z \\
T_{\theta\theta} &= c_{12}^D S_{rr} + c_{11}^D S_{\theta\theta} + c_{13}^D S_{zz} - h_{31} D_z \\
T_{zz} &= c_{13}^D S_{rr} + c_{13}^D S_{\theta\theta} + c_{33}^D S_{zz} - h_{33} D_z \\
E_z &= -h_{31} S_{rr} - h_{31} S_{\theta\theta} - h_{33} S_{zz} + D_z / \varepsilon_{33}^S
\end{aligned}
\tag{1}
$$

The strain tensor S in terms of displacements (u) in the polar coordinate system is defined by:

$$
S = \begin{bmatrix} S_{rr} & 0 & 0 \\ 0 & S_{\theta\theta} & 0 \\ 0 & 0 & S_{zz} \end{bmatrix} = \begin{bmatrix} \partial u_r / \partial r & 0 & 0 \\ 0 & u_r / r & 0 \\ 0 & 0 & \partial u_z / \partial z \end{bmatrix}
\tag{2}
$$

The differential equations governing the vibrations of an elastic body in the radial and thickness directions can also be applied, with reasonable approximation, to a piezoceramic ring. These equations are derived from the equilibrium equations [11, 25]:

$$
\frac{\partial T_{rr}}{\partial r} + \frac{T_{rr} - T_{\theta\theta}}{r} = \rho \frac{\partial^2 u_r}{\partial t^2}, \quad \frac{\partial T_{zz}}{\partial z} = \rho \frac{\partial^2 u_z}{\partial t^2}
\tag{3}
$$

By substituting Eq. (2) into Eq. (1) and then substituting the resulting equations into Eq. (3), the differential equations of vibrations in the radial and thickness directions are obtained as:

$$c_{11}^D \left(\frac{\partial^2 u_r}{\partial r^2} + \frac{1}{r}\frac{\partial u_r}{\partial r} - \frac{u_r}{r^2} \right) = \rho \frac{\partial^2 u_r}{\partial t^2}, c_{33}^D \frac{\partial^2 u_z}{\partial z^2} = \rho \frac{\partial^2 u_z}{\partial t^2} \tag{4}$$

The solution to the above equations represents the displacement components of the ring in the radial and thickness directions and is assumed to be in the form of two orthogonal wave functions as shown below:

$$\begin{aligned} u_r(r,t) &= [AJ_1(k_r r) + BY_1(k_r r)]\, e^{j\omega t} \\ u_z(z,t) &= [C\sin(k_z r) + D\cos(k_z z)]\, e^{j\omega t} \end{aligned} \tag{5}$$

where, $k_r = \omega/v_r$, $k_z = \omega/v_z$, $v_r = \sqrt{c_{11}^D/\rho}$ and $v_z = \sqrt{c_{33}^D/\rho}$ are the wave numbers and phase velocities of the radial and thickness modes, respectively. The constants A, B, C, and D in the above equations are calculated under the assumption of continuity of the surface velocities of the piezoceramic ring and using the boundary conditions. The boundary conditions are as follows:

$$\begin{aligned} \left.\frac{\partial u_r}{\partial t}\right|_{r=b} &= v_1 e^{j\omega t}, \quad \left.\frac{\partial u_r}{\partial t}\right|_{r=a} = -v_2 e^{j\omega t} \\ \left.\frac{\partial u_z}{\partial t}\right|_{z=h} &= -v_3 e^{j\omega t}, \quad \left.\frac{\partial u_z}{\partial t}\right|_{z=-h} = v_4 e^{j\omega t} \end{aligned} \tag{6}$$

By applying the boundary conditions to the orthogonal wave functions, the constants A, B, C, and D are obtained as follows:

$$\begin{aligned} A &= \frac{A_1 v_1 + A_2 v_2}{j\omega}, \quad B = \frac{B_1 v_1 + B_2 v_2}{j\omega} \\ C &= -\frac{v_3 + v_4}{2j\omega \sin(k_z h)}, \quad D = \frac{v_4 - v_3}{2j\omega \cos(k_z h)} \end{aligned} \tag{7}$$

where, the relations (8) are valid:

$$\begin{aligned} A_1 &= \frac{Y_1(k_r a)}{J_1(k_r b)Y_1(k_r a) - J_1(k_r a)Y_1(k_r b)} \\ A_2 &= \frac{Y_1(k_r b)}{J_1(k_r b)Y_1(k_r a) - J_1(k_r a)Y_1(k_r b)} \\ B_1 &= \frac{J_1(k_r a)}{J_1(k_r a)Y_1(k_r b) - J_1(k_r b)Y_1(k_r a)} \\ B_2 &= \frac{J_1(k_r b)}{J_1(k_r a)Y_1(k_r b) - J_1(k_r b)Y_1(k_r a)} \end{aligned} \tag{8}$$

For modeling the behavior of the ring, it is assumed that Eq. (9) between the stresses and forces applied to the surfaces of the ring are valid [26]:

$$\begin{aligned} \int_{P_1} T_{rr}(b)dP &= -F_1 \\ \int_{P_2} T_{rr}(a)dP &= -F_2 \\ \int_{P_3} T_z(h)dP &= -F_3 \\ \int_{P_4} T_{zz}(-h)dP &= -F_4 \end{aligned} \tag{9}$$

where, P_1 and P_2 represent the inner and outer lateral surfaces, respectively, and P_3 and P_4 represent the annular surfaces of the ring with coordinates $z = h$ and $z = -h$, then, Eq. (10) are obtained [14]:

$$
\begin{aligned}
2\pi b \int_{-h}^{h} T_{rr}(b) dz &= -F_1 \\
2\pi a \int_{-h}^{h} T_{rr}(a) dz &= -F_2 \\
2\pi \int_{b}^{a} T_{=}(h) r dr &= -F_3 \\
2\pi \int_{b}^{a} T_{=}(-h) r dr &= -F_4
\end{aligned}
\tag{10}
$$

In addition, Eq. (11) represents the relationship between current and electric displacement in the z-direction:

$$
I = 2\pi \int_{b}^{a} \frac{\partial D_z}{\partial t} r dr = j\omega\pi \left(a^2 - b^2 \right) D_0 e^{j\omega t} = j\omega\pi \left(a^2 - b^2 \right) D_z
\tag{11}
$$

Therefore, D_z is obtained as follows:

$$
D_z = I / \left[j\omega\pi \left(a^2 - b^2 \right) \right]
\tag{12}
$$

The result of expression (10) is a system of linear equations, which can also be represented in matrix form as shown in Eq. (13):

$$
\begin{bmatrix} F_1 \\ F_2 \\ F_3 \\ F_4 \\ V \end{bmatrix} =
\begin{bmatrix}
z_{11} & z_{12} & z_{13} & z_{13} & z_{15} \\
z_{21} & z_{22} & z_{23} & z_{23} & z_{25} \\
z_{13} & z_{23} & z_{33} & z_{34} & z_{35} \\
z_{13} & z_{23} & z_{34} & z_{33} & z_{35} \\
z_{15} & z_{25} & z_{35} & z_{35} & z_{55}
\end{bmatrix}
\begin{bmatrix} v_1 \\ v_2 \\ v_3 \\ v_4 \\ I \end{bmatrix}
\tag{13}
$$

The impedance matrix elements are also defined as:

$$
\begin{aligned}
z_{11} &= \frac{-4\pi h}{j\omega} \left\{ c_{12}^D - c_{11}^D \left[1 - k_r b \left(A_1 J_0 \left(k_r b \right) + B_1 Y_0 \left(k_r b \right) \right) \right] \right\} \\
z_{22} &= \frac{4\pi h}{j\omega} \left\{ c_{12}^D - c_{11}^D \left[1 + k_r a \left(A_2 J_0 \left(k_r a \right) + B_2 Y_0 \left(k_r a \right) \right) \right] \right\} \\
z_{12} &= \frac{-4\pi k_r b h c_{11}^D}{j\omega} \left[A_2 J_0 \left(k_r b \right) + B_2 Y_0 \left(k_r b \right) \right] \\
z_{21} &= \frac{-4\pi k_r a h c_{11}^D}{j\omega} \left[A_1 J_0 \left(k_r a \right) + B_1 Y_0 \left(k_r a \right) \right] \\
z_{13} &= \frac{2\pi b c_{13}^D}{j\omega}, \quad z_{15} = \frac{4\pi b h h_{31}}{j\omega P} \\
z_{23} &= \frac{2\pi a c_{13}^D}{j\omega}, \quad z_{25} = \frac{4\pi a h h_{31}}{j\omega P} \\
z_{33} &= \frac{c_{33}^D k_z P}{j\omega \tan \left(2k_z h \right)}, \quad z_{34} = \frac{c_{33}^D k_z P}{j\omega \sin \left(2k_z h \right)} \\
z_{35} &= \frac{h_{33}}{j\omega}, \quad z_{55} = \frac{1}{j\omega C_0}
\end{aligned}
\tag{14}
$$

where, $P = \pi \left(a^2 - b^2 \right)$ is the area of the ring and $C_0 = \left(\varepsilon_{33}^S P \right) / (2h)$ is the piezoceramic capacitance at constant strain (known as clamped capacitance). None of the elements of the impedance matrix are zero. This means that the voltage V and each of the forces applied to the surfaces of the ring depend on the velocity of all surfaces and the current I. Finally, after applying the alternating voltage $V = V_0 e^{j\omega t}$, the behavior of the piezoceramic ring can be analyzed using the matrix equation, and the input electrical impedance can be obtained using the formula $Z = V/I$.

2.2 Mancic's Matrix Model for Metallic Rings

Using Mancic's model, a three-dimensional representation of metallic rings and discs can also be obtained [27]. The mentioned metallic ring is illustrated in Figure 5. vi and Fi, respectively, represent the velocities and forces applied on the surfaces.
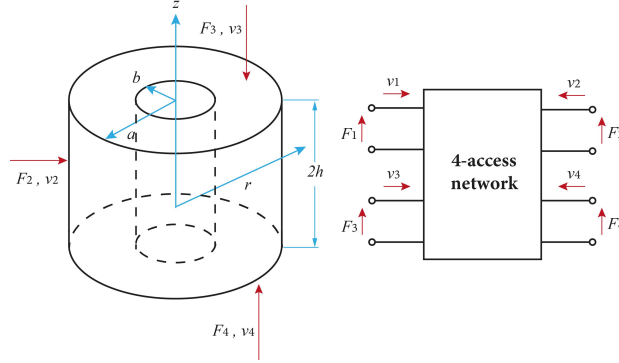
Figure 5. Mancic's matrix model for metallic rings

This model is obtained by neglecting the piezoelectric constants h_{31} and h_{33} in Eq. (14). Moreover, given the isotropic nature of the metal, the following relations are obtained:

$$c_{11} = c_{33} = \lambda_m + 2\mu \quad c_{12} = c_{13} = \lambda_m \tag{15}$$

where, λ_m and μ are Lamé constants as follows:

$$\lambda_m = \frac{vE_Y}{(1+v)(1-2v)} \quad \mu = \frac{E_Y}{2(1+v)} \tag{16}$$

Finally, the matrix equations of the metallic ring are obtained in the form of Eq. (17):

$$
\begin{bmatrix} F_1 \\ F_2 \\ F_3 \\ F_4 \end{bmatrix} =
\begin{bmatrix}
z_{11} & z_{12} & z_{13} & z_{13} \\
z_{21} & z_{22} & z_{23} & z_{23} \\
z_{13} & z_{23} & z_{33} & z_{34} \\
z_{13} & z_{23} & z_{34} & z_{33}
\end{bmatrix}
\begin{bmatrix} v_1 \\ v_2 \\ v_3 \\ v_4 \end{bmatrix}
\tag{17}
$$

and the elements of the impedance matrix are also obtained as:

$$
\begin{aligned}
z_{11} &= \frac{-4\pi h}{j\omega} \left\{ c_{12} - c_{11} \left[1 - kb \left(A_1 J_0(kb) + B_1 Y_0(kb) \right) \right] \right\} \\
z_{22} &= \frac{4\pi h}{j\omega} \left\{ c_{12} - c_{11} \left[1 + ka \left(A_2 J_0(ka) + B_2 Y_0(ka) \right) \right] \right\} \\
z_{12} &= \frac{-4\pi kbhc_{11}}{j\omega} \left[A_2 J_0(kb) + B_2 Y_0(kb) \right] \\
z_{21} &= \frac{-4\pi kahc_{11}}{j\omega} \left[A_1 J_0(ka) + B_1 Y_0(ka) \right] \\
z_{13} &= \frac{2\pi bc_{12}}{j\omega}, \quad z_{23} = \frac{2\pi ac_{12}}{j\omega} \\
z_{33} &= \frac{c_{11}k\pi \left(a^2 - b^2 \right)}{j\omega \tan(2kh)}, \quad z_{34} = \frac{c_{11}k \left(a^2 - b^2 \right)}{j\omega \sin(2kh)}
\end{aligned}
\tag{18}
$$

The values of the constants A_1, A_2, B_1, and B_2 are calculated using the boundary conditions presented as:

$$
\begin{aligned}
A_1 &= \frac{Y_1(ka)}{J_1(kb)Y_1(ka) - J_1(ka)Y_1(kb)} \quad & B_1 &= \frac{J_1(ka)}{J_1(ka)Y_1(kb) - J_1(kb)Y_1(ka)} \\
A_2 &= \frac{Y_1(kb)}{J_1(kb)Y_1(ka) - J_1(ka)Y_1(kb)} \quad & B_2 &= \frac{J_1(kb)}{J_1(ka)Y_1(kb) - J_1(kb)Y_1(ka)}
\end{aligned}
\tag{19}
$$

2.3 Matrix Model of a Tonpilz Transducer

Matrix models are essentially simplified versions of distributed models, which themselves originate from lumped parameter models. By dividing the body into n equal elements, its equations of motion can be derived along direction z. Each element is modeled as a mass $M = \rho A_0 \Delta z$ connected to a spring with stiffness $K = Y A_0 / \Delta z$ and length $\Delta z = L/n$. The displacement of each element is denoted by ζ_i. The equivalent mass-spring system representing the body is illustrated in Figure 6.
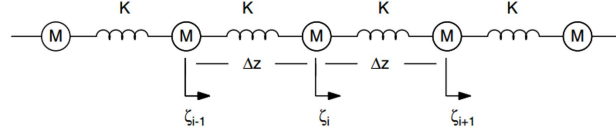
Figure 6. Equivalent mass-spring system of the rod [28]

According to Figure 6, the equation of motion for body i is obtained as:

$$M \frac{\partial^2 \zeta_i}{\partial t^2} = -K \left(\zeta_i - \zeta_{i-1} \right) - K \left(\zeta_i - \zeta_{i+1} \right) \tag{20}$$

where, $K/M = Y/\rho(\Delta z)^2$ and one gets:

$$M \frac{\partial^2 \zeta_i}{\partial t^2} = \frac{Y}{\rho} \frac{\left(\zeta_{i+1} - \zeta_i \right)/\Delta z - \left(\zeta_i - \zeta_{i-1} \right)/\Delta z}{\Delta z} \tag{21}$$

In Eq. (21), if Δz tends to zero, the difference between the displacements also approaches zero, and the wave Eq. (22) is obtained [4]:

$$\frac{\partial^2 \zeta}{\partial t^2} = c^2 \frac{\partial^2 \zeta}{\partial z^2} \tag{22}$$

where, $c = (Y/\rho)^2$ is the longitudinal wave propagation velocity of the material, and Y is Young's modulus. The value of c for steel and aluminum is 5100 m/s while for piezoelectric materials, it is 3000 m/s. Considering that the analysis is typically performed in the frequency domain, the solution to the one-dimensional wave equation can be written in the form of Eq. (23) where $k = \omega/c$. is the wave number:

$$\zeta(z,t) = \zeta(z)e^{j\omega t} = Be^{-j(kz-\omega t)} + De^{j(kz+\omega t)} \tag{23}$$

Thereby, the relationships for the velocity of each element, $u = \partial \zeta / \partial t$, and the force applied to them, $F = -A_0 T = -A_0 Y \partial \zeta / \partial z$, are obtained by Eq. (24):

$$
\begin{aligned}
u(z) &= j\omega \zeta(z) = j\omega \left[Be^{-jk} + De^{jk} \right] \\
F(z) &= -jkY A_0 \left[Be^{-jkk} - De^{jk} \right]
\end{aligned}
\tag{24}
$$

The parameters B and D are constant and calculated using the boundary conditions at both ends of the body. For example, the boundary conditions can be expressed as $F = 0$ or $u = 0$, or more generally as $F_i/u_i = Z_i$. The mechanical impedance at both ends of the body is Z_i. The mechanical impedance $Z(z) = F(z)/u(z)$ can be calculated at all points along the body as follows:

$$Z(z) = \rho c A_0 \frac{\left[Be^{-jkt} - De^{jkt} \right]}{\left[Be^{-jkt} + De^{jkt} \right]} \tag{25}$$

If the impedance values at z = 0 and z = L are denoted by Z_Ω and Z_L, respectively, Eq. (25) will transform into:

$$Z_0 = \rho c A_0 \frac{\left[Z_L + \rho c A_0 \tan kL \right]}{\left[\rho c A_0 + j Z_L \tan kL \right]} \tag{26}$$
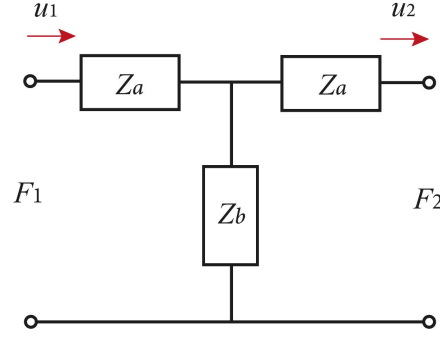
Figure 7. Equivalent circuit of a long rod

It can be demonstrated through algebraic operations that Eq. (26) is equivalent to the circuit shown in Figure 7 [4]. Then, the governing equation can be written in matrix form as:

$$\begin{bmatrix} F_0 \\ F_L \end{bmatrix} = \begin{bmatrix} z_a & -z_b \\ z_b & -z_a \end{bmatrix} \begin{bmatrix} u_0 \\ u_L \end{bmatrix}$$

$$z_a = -i\rho cA \cot(kL), z_b = -i\rho cA \sin(kL)$$

(27)

Now, using the aforementioned model for a single rod, it is also possible to model systems consisting of multiple rods connected in series—provided that the cross-sectional area of all rods is very small compared to their length. These rods are not necessarily of the same material [28]. The frequency response of this system at its two ends is obtained by simultaneously solving the matrix equations corresponding to each rod, as shown in Eq. (28). The internal forces at the junction of any two consecutive members are equal:

$$\begin{bmatrix} F_{1s} \\ F_{1e} \end{bmatrix} = \begin{bmatrix} z_{1a} & -z_{1b} \\ z_{1b} & -z_{1a} \end{bmatrix} \begin{bmatrix} u_{1s} \\ u_{1e} \end{bmatrix} \quad \begin{bmatrix} F_{2s} \\ F_{2e} \end{bmatrix} = \begin{bmatrix} z_{2a} & -z_{2b} \\ z_{2b} & -z_{2a} \end{bmatrix} \begin{bmatrix} u_{2s} \\ u_{2e} \end{bmatrix}$$

$$\begin{bmatrix} F_{3s} \\ F_{3e} \end{bmatrix} = \begin{bmatrix} z_{3a} & -z_{3b} \\ z_{3b} & -z_{3a} \end{bmatrix} \begin{bmatrix} u_{3s} \\ u_{3e} \end{bmatrix}$$

$$F_{1e} = F_{2s} u_{1e} = u_{2s}$$

$$F_{2e} = F_{3s} u_{2e} = u_{3s}$$

(28)

By incorporating piezoelectric constants and an electrical port in addition to mechanical ports, a similar matrix model can be derived for piezoceramic materials. Then, by connecting the various components of a Tonpilz transducer together and applying the correct boundary conditions, the matrix equations corresponding to the transducer can be obtained [29].

2.4 Finite Element Analysis

The finite element method is fundamentally based on dividing a body into a finite number of elements and combining their solutions to obtain the solution to the whole problem. The greater the number of elements, the more accurate the results, bringing them closer to exact solution. In analytical methods, many simplifications are applied to the problem, and some assumptions are incorporated into the solution. However, numerical methods are highly time-consuming, and to study the effect of design parameter changes on transducer performance, these lengthy calculations must be repeated each time. Therefore, analytical methods with lower computational costs are typically used to examine the effects of system parameters.

Finite element analysis is performed in three stages. In the first stage, the problem's geometry, material properties, element types, and boundary conditions (constraints and applied forces) are defined. In the second stage, the matrix equations for all elements are assembled into a global matrix according to finite element method rules and solved simultaneously. In the final stage, the obtained data is processed, and the resulting plots are generated. Each element, depending on its shape and type, has a certain number of nodes, and computations are performed at these nodes. The matrix equation for each node related to the metallic and isotropic components of the transducer is given by:

$$\left[[K] - \omega^2 [M] \right] \{x\} = \{F\}$$

(29)

where, K is the stiffness matrix, M is the mass matrix, and x and F are the displacement and force vectors, respectively. For nodes in the acoustic domain, the same equation is used with the pressure vector replacing the displacement vector. The matrix equations for nodes corresponding to piezoceramic rings are given as follows:

$$\begin{bmatrix} \left[K^E\right] + j\omega[R] - \omega^2[M] & -[N] \\ [N]^t & \left[C^S\right] \end{bmatrix} \left\{ \begin{array}{c} x \\ V \end{array} \right\} = \left\{ \begin{array}{c} \{F\} \\ \{Q\} \end{array} \right\} \tag{30}$$

where, K^E is the stiffness matrix under constant electric field (short-circuit condition), R is the resistance, C^S is the piezoelectric capacitance matrix under constant strain boundary conditions, V and Q are the voltage and electric charge vectors, respectively, N is the matrix that, like the electromechanical coupling factor, relates the piezoelectric's electrical and mechanical parameters [30–32].

2.5 Simulation of a Tonpilz Transducer in COMSOL

One of the useful software packages for array simulation is COMSOL Multiphysics. COMSOL enables the combination of different physics to simulate complex physical problems. In this software, a model can include one or multiple physics interfaces to simulate all real-world interactions. In this study, a single Tonpilz transducer is first simulated in COMSOL and analyzed within the frequency range of 10 to 30 kHz. The effect of applied stress on the bolt is neglected in this model.

Given the transducer's axial symmetry, a 2D cross-section can first be drawn as shown in Figure 8, then revolved around the z-axis to obtain the complete 3D geometry. As illustrated, an infinite water domain is defined in front of the head mass, and finally, a perfectly matched layer (PML) is added to absorb acoustic waves and prevent their reflection back toward the transducer [33].
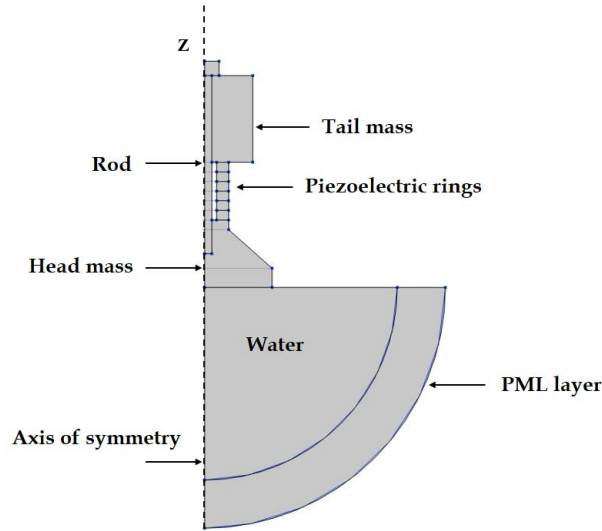
Figure 8. The cross-sectional area of the simulated Tonpilz transducer in COMSOL
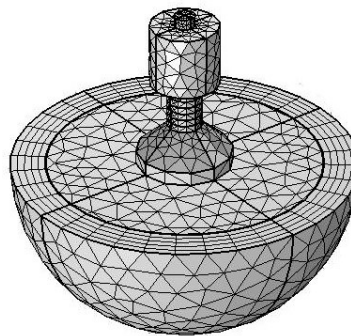
Figure 9. Meshed Tonpilz transducer in COMSOL

In the next step, boundary conditions are defined. In the acoustic interface, a boundary integral is implemented at the water-PML interface to calculate far-field sound pressure and ultimately plot the radiation pattern. In the solid

mechanics interface, the transducer is fixed by applying a rigid constraint to the tail mass's outer surface. In the electrostatics interface, each piezoceramic ring is excited with an RMS voltage of 1 volt. To ensure the piezoceramic rings collectively achieve maximum possible displacement, their strain must be in phase. This requires adjacent piezoceramic rings to have opposite polarization directions, necessitating the definition of a new coordinate system for proper polarization orientation.

In this modeling, the head mass is made of aluminum, the tail mass and bolt are steel, and the piezoelectric rings are PZT8. After material selection, the entire model is meshed (Figure 9). For proper acoustic analysis, the acoustic region must be meshed such that the size of generated elements is smaller than 0.2 times the smallest wavelength. The smallest wavelength is obtained by dividing the speed of sound in water by the maximum frequency in the studied frequency range. After final processing of the obtained data, the variations of the transmitted voltage response, input electrical impedance, and beam pattern are generated.

2.6 Modeling of Planar Arrays in COMSOL

Given that accurate identification and estimation of bandwidth is crucial for the precision and performance efficiency of ultrasonic transducers, and considering the high manufacturing costs of these transducers and arrays, the use of finite element method (FEM) and boundary element method (BEM) appears highly advantageous [34]. Planar arrays represent the simplest type of arrays. This paper analyzes the frequency-domain behavior of several planar arrays with square, diamond, and circular configurations, while investigating the effects of varying the number of transducers and their arrangement on wave angle and array bandwidth. Each array is housed in a metallic enclosure, with rigid wall boundary conditions applied to the enclosure in the acoustic interface. The spacing between transducers in all three structures is set at half the acoustic wavelength ($\lambda/2$) [4, 35].

The modeling procedure follows a similar approach to that of a Tonpilz transducer, with the difference being the selection of the Pressure Acoustics, Boundary Elements (PABE) physics environment. Initially, the array can be modeled and solved without considering the acoustic interface or the coupling between the active surface and the acoustic medium, allowing for initial stress calculations within the array. Subsequently, full calculations can be performed by incorporating the previously omitted interface and coupling, yielding results for electrical impedance, transmitted voltage response, and beam pattern. Figure 10 illustrates the simulated square array configuration.

Another type of planar array has a circular configuration with radius a. Figure 11 shows this array configuration. The distance between the centers of any two adjacent transducers is $\lambda/2$, and the number of transducers is N. N must be a multiple of 4. In this case, the angle between any two elements is calculated as follows:

$$\phi = \frac{360}{N} \tag{31}$$
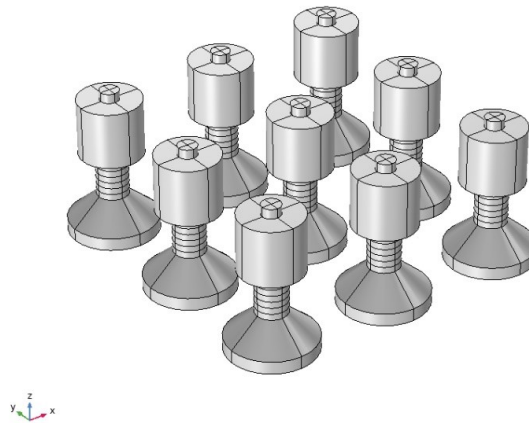
Figure 10. Square array simulated in COMSOL

In this case, the far-field regions are identical for both xz and yz planes, as well as any plane passing through both transducers and the array center. Furthermore, by rotating the square array by 45 degrees, a diamond-shaped array can be obtained. As shown in Figure 12, the distance between the centers of two adjacent elements was S before rotation and becomes $S/\sqrt{2}$ after rotation.
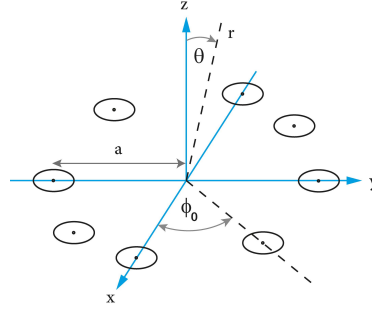
Figure 11. Circular-shape planar array
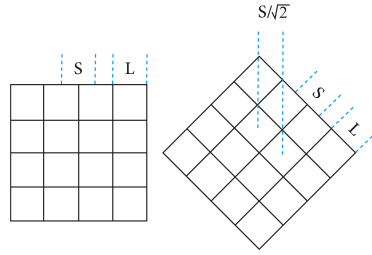
Figure 12. Diamond-shape planar array

3 Results, Data Analysis, and Discussion

In the first stage of result analysis, a Tonpilz transducer was simulated in three dimensions using the Mancic matrix model. In the second stage, a Tonpilz transducer was simulated using COMSOL Multiphysics software. Subsequently, multiple transducers were arranged in circular, square, and diamond planar configurations, and the resulting arrays were also simulated. Finally, the electrical input impedance, transmitted voltage response, and beam patterns of the arrays were analyzed and compared.

3.1 Simulation of a Piezoceramic Ring

In this section, the input electrical impedance plots along with resonance and anti-resonance frequencies obtained from simulations of a piezoceramic ring are compared between Mancic's matrix model and the finite element model. The simulated ring is made of PZT8 and is polarized along its thickness direction. It is known that the force applied to each surface of the piezoceramic ring is calculated from $F_i = -Z_i v_i$, where Z_i is the characteristic impedance applied to these surfaces and v_i is the velocity of these surfaces. The characteristic impedance is obtained by multiplying the acoustic impedance by the surface area. Using Eqs. (13) and (14), one can write:

$$
\begin{bmatrix} 0 \\ 0 \\ 0 \\ 0 \\ V \end{bmatrix} = \begin{bmatrix} z_{11}+Z_1 & z_{12} & z_{13} & z_{13} & z_{15} \\ z_{21} & z_{22}+Z_2 & z_{23} & z_{23} & z_{25} \\ z_{13} & z_{23} & z_{33}+Z_3 & z_{34} & z_{35} \\ z_{13} & z_{23} & z_{34} & z_{33}+Z_4 & z_{35} \\ z_{15} & z_{25} & z_{35} & z_{35} & z_{55} \end{bmatrix} \begin{bmatrix} v_1 \\ v_2 \\ v_3 \\ v_4 \\ I \end{bmatrix}
$$
$$
= \begin{bmatrix} A_{11} & A_{12} & A_{13} & A_{14} & A_{15} \\ A_{21} & A_{22} & A_{23} & A_{24} & A_{25} \\ A_{31} & A_{32} & A_{33} & A_{34} & A_{35} \\ A_{41} & A_{42} & A_{43} & A_{44} & A_{45} \\ A_{51} & A_{52} & A_{53} & A_{54} & A_{55} \end{bmatrix} \begin{bmatrix} v_1 \\ v_2 \\ v_3 \\ v_4 \\ I \end{bmatrix}
\tag{32}
$$

After some algebraic computations, one obtains:

$$
\begin{bmatrix} 0 \\ 0 \\ 0 \\ 0 \\ E_5 \end{bmatrix} = \begin{bmatrix} A_{11} & A_{12} & A_{13} & A_{14} & A_{15} \\ 0 & a_{11} & a_{12} & a_{13} & a_{14} \\ 0 & 0 & b_{11} & b_{12} & b_{13} \\ 0 & 0 & 0 & c_{11} & c_{12} \\ 0 & 0 & 0 & c_{21} & c_{22} \end{bmatrix} \begin{bmatrix} v_1 \\ v_2 \\ v_3 \\ v_4 \\ I \end{bmatrix}
\tag{33}
$$

145

where, the elements of the square matrix are calculated as:

$$
\begin{aligned}
a_{i,j} &= A_{1,j+1} \cdot A_{i+1,1} - A_{1,1} \cdot A_{i+1,j+1} &&(i,j = 1,2,3,4) \\
b_{i,j} &= a_{1,j+1} \cdot a_{i+1,1} - a_{1,1} \cdot a_{i+1,j+1} &&(i,j = 1,2,3) \\
c_{i,j} &= b_{1,j+1} \cdot b_{i+1,1} - b_{1,1} \cdot b_{i+1,j+1} &&(i,j = 1,2) \\
E_5 &= -A_{11} \cdot a_{11} \cdot b_{11} \cdot V
\end{aligned}
\tag{34}
$$

To set the matrix element A_{21} equal to zero, as presented in Eq. (35), the second row of matrix A must first be multiplied by $-A_{11}$. Then, this row should be added to the first row of matrix A multiplied by A_{21}:

$$
\begin{bmatrix}
A_{11} & A_{12} & A_{13} & A_{14} & A_{15} \\
A_{11}A_{21} - A_{11}A_{21} & A_{12}A_{21} - A_{11}A_{22} & A_{13}A_{21} - A_{11}A_{23} & A_{14}A_{21} - A_{11}A_{24} & A_{15}A_{21} - A_{11}A_{25} \\
A_{31} & A_{32} & A_{33} & A_{34} & A_{35} \\
A_{41} & A_{42} & A_{43} & A_{44} & A_{45} \\
A_{51} & A_{52} & A_{53} & A_{54} & A_{55}
\end{bmatrix}
$$
$$
=
\begin{bmatrix}
A_{11} & A_{12} & A_{13} & A_{14} & A_{15} \\
0 & a_{11} & a_{12} & a_{13} & a_{14} \\
A_{31} & A_{32} & A_{33} & A_{34} & A_{35} \\
A_{41} & A_{42} & A_{43} & A_{44} & A_{45} \\
A_{51} & A_{52} & A_{53} & A_{54} & A_{55}
\end{bmatrix}
\tag{35}
$$

For the analytical solution of the piezoceramic ring and obtaining the electrical impedance plot, Simulink toolbox in MATLAB software was utilized. For this purpose, two blocks are defined. The first block calculates the components of matrix (34) using piezoelectric constants and ring dimensions provided as inputs to the model. This requires Bessel functions to be defined as extrinsic functions. Since all parameters are predefined, no algebraic loops occur in this model. The second block solves Eq. (34) using the values obtained from the first block and computes the input electrical impedance $Z = V/I$. Figure 13 shows this block [24].
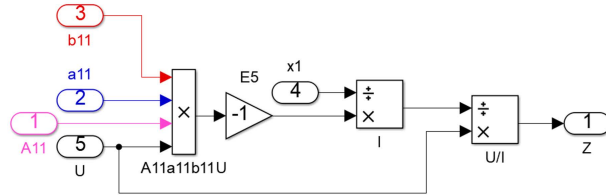
**Figure 13.** Calculation of input electrical impedance in Block 2 [24]

After calculating Z, the input electrical impedance in decibel scale is computed as:

$$
z = 20 \log \left(\frac{Z}{50} + 1 \right)
\tag{36}
$$

where, z is the input electrical impedance in decibel scale. Additionally, since the simulated ring vibrates in air independently, the acoustic impedance value on all its surfaces will be 400 $\mathrm{kg/m^2}$ s. Figure 14 shows the simulation results of a ring obtained using both MATLAB and COMSOL software. The simulated ring is made of PZT8 material, with an inner radius of 2 mm, outer radius of 5 mm, and thickness of 2 mm.

As illustrated in Figure 14, one of the vibrational modes is the thickness vibration mode (T), while the remaining modes are radial vibration modes (R). Frequency constants and semi-empirical relationships are used to identify different vibration modes. According to this figure reveals that the matrix model can predict the first thickness mode (T_1) and first radial mode (R_1) with appropriate accuracy. Since these two modes have the most significant industrial applications, this model can serve as a practical tool for transducer design and optimization.

Table 1 presents the resonance and anti-resonance frequencies obtained through both matrix and finite element models for the first thickness mode (T_1) and first two radial modes (R_1 and R_2). The observed computational error arises because the matrix model only accounts for thickness and radial vibration modes. Furthermore, shear vibration modes are absent in the output of the matrix model.
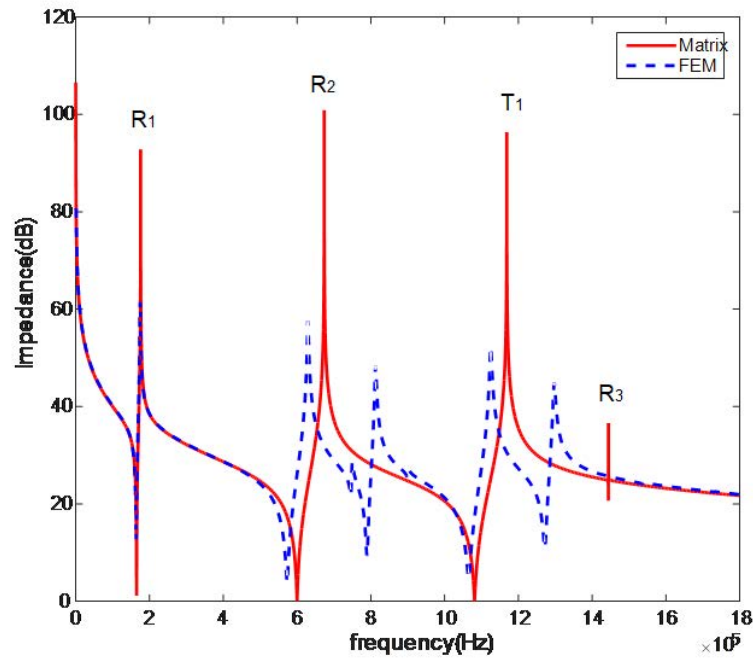
Figure 14. Input electrical impedance diagram of a piezoceramic ring

Table 1. Matrix model error in measuring piezoceramic ring electrical impedance

	Thickness Vibration Mode Frequency	The First Radial Vibration Mode Frequency	The Second Radial Vibration Mode Frequency	Units
FE model	1125	175	629	kHz
Matrix model	1168	175.8	673.6	kHz
The error of Matrix model (%)	3.8	0.46	7	-

Table 2. Calculation of matrix model error in resonant frequency measurement of Tonpilz transducers

	FE Model	Matrix Model	Error (%)
Resonance frequency	18.1	19.4	7

3.2 Simulation of Tonpliz Transducer

3.2.1 Matrix model

In this section, the Tonpilz transducer model in Nouri et al.'s study [5] with an operating frequency of 18 kHz is simulated using the Jovanovic matrix model [29] and MATLAB's Simulink tool. This model accounts for both thickness and radial vibration modes as well as their coupling effects. Consequently, it can serve as an accurate and reliable method for designing Tonpilz transducers. Figure 15 displays the electrical impedance diagram obtained for the Tonpilz transducer using the Mancic matrix model. Figure 16 additionally presents the electrical impedance plot derived through the finite element method.

The results of resonant frequency of Tonpilz transducer using the matrix model and finite element model are reported in Table 2. The 7% error discrepancy originates from the generalized assumptions in the matrix model, including: simplification of the head mass geometry, the piezoelectric constants employed, and the use of two piezoceramic rings instead of six. Both models neglect mechanical and dielectric losses. Currently, no ideal analytical model exists that can simultaneously incorporate all parameters, boundary conditions, and other transducer performance dependencies while predicting all resonant modes. Therefore, the Mancic model can be regarded as the most efficient model for analyzing the sandwich-type transducers.
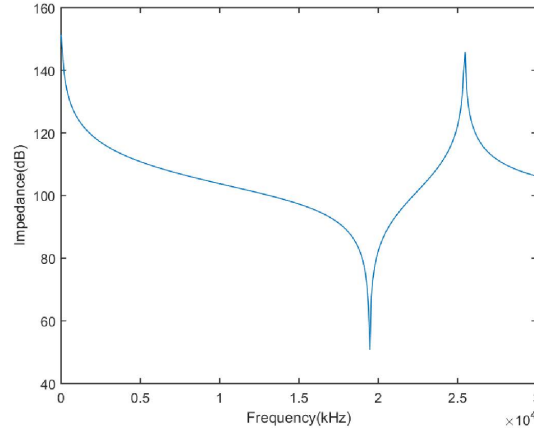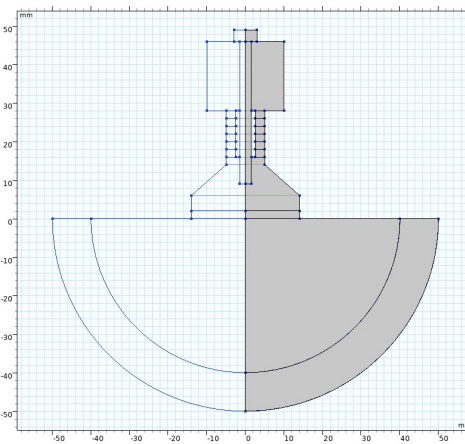
Figure 15. Electrical impedance plot of the Tonpilz transducer using the Mancic matrix model
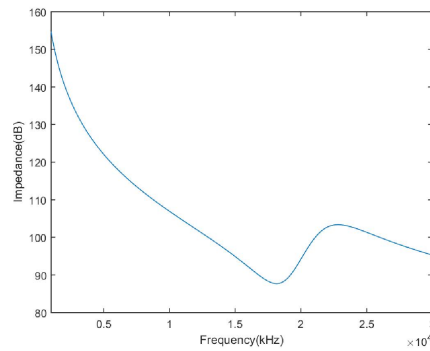
Figure 16. Electrical impedance plot of the Tonpilz transducer using the finite element method

3.3 Finite Element Modeling

In sonar systems, transducer arrays and their associated electronic circuits are encapsulated and protected using various methods [34]. Among the most common encapsulating materials are polyurethane, corprene and silicone rubber [35]. The following section presents simulation results of the Tonpilz transducer in COMSOL software. In this model, a thin polyurethane layer has been incorporated adjacent to the active surface. Figure 17 shows a view of this Tonpilz transducer model. For simplicity, the electrodes between the piezoceramic rings have been omitted.

Figure 17. Schematic representation of the polyurethane-coated Tonpilz transducer within its acoustic domain

Figure 18 shows the transducer's input electrical impedance results. As can be observed, the minimum electrical impedance occurs at approximately 16.5 kHz, while the maximum appears near 20.5 kHz. These frequencies represent

the resonance and anti-resonance frequencies, respectively. No other resonant modes are visible within this frequency range.
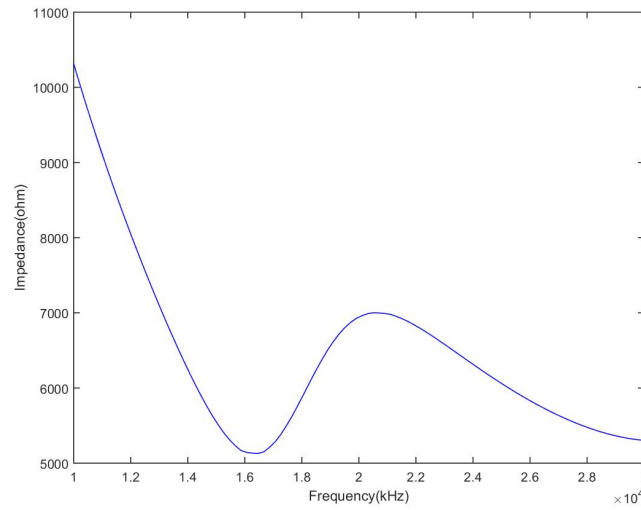

**Figure 18.** Electrical impedance diagram of the polyurethane-coated Tonpilz transducer
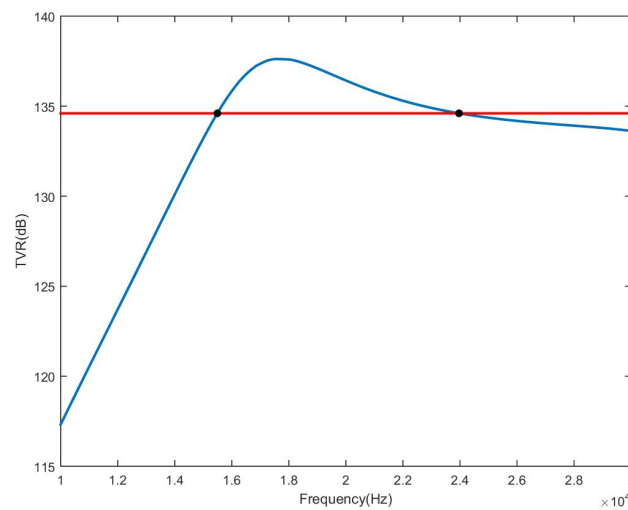
Figure 19. Output voltage response of the polyurethane-coated Tonpilz transducer

The transducer's output voltage response is presented in Figure 19. While the peak output voltage response was expected to occur at the resonance frequency, a slight frequency shift is evident. The maximum output voltage response actually occurs at approximately 17.5 kHz. This discrepancy results from the emergence of a vibrational mode that creates a phase difference between the motion of the edges and the center of head mass, consequently reducing the average velocity and output voltage response.

This diagram can be used to calculate the transducer's bandwidth. A larger bandwidth value indicates the transducer can operate over a wider frequency range. As shown in Figure 19, the resulting bandwidth is 8.5 kHz. Figure 20 displays the displacement of transducer components at its resonance frequency. As evident, the tail mass exhibits the smallest displacement while the head mass shows the largest displacement. In fact, at the transducer's resonance frequency, it stretches uniformly from the head mass side. Figure 21 shows the beam pattern of the transducer. This plot can be used to calculate the beamwidth. As previously mentioned, the beamwidth represents the angular width where maximum radiated power is emitted. In this case, the beamwidth is approximately 82.5 degrees.
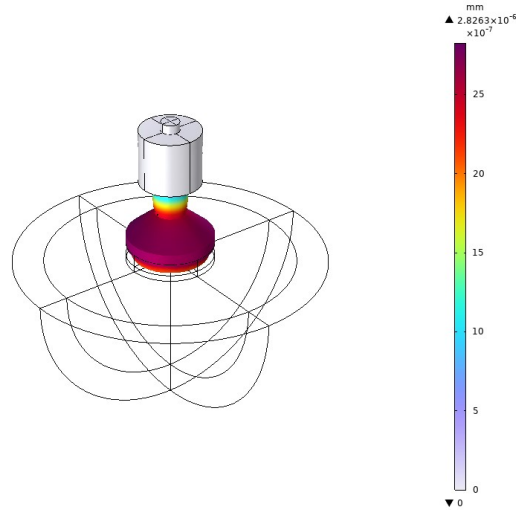
**Figure 20.** Displacement of the Tonpilz transducer components at its resonance frequency
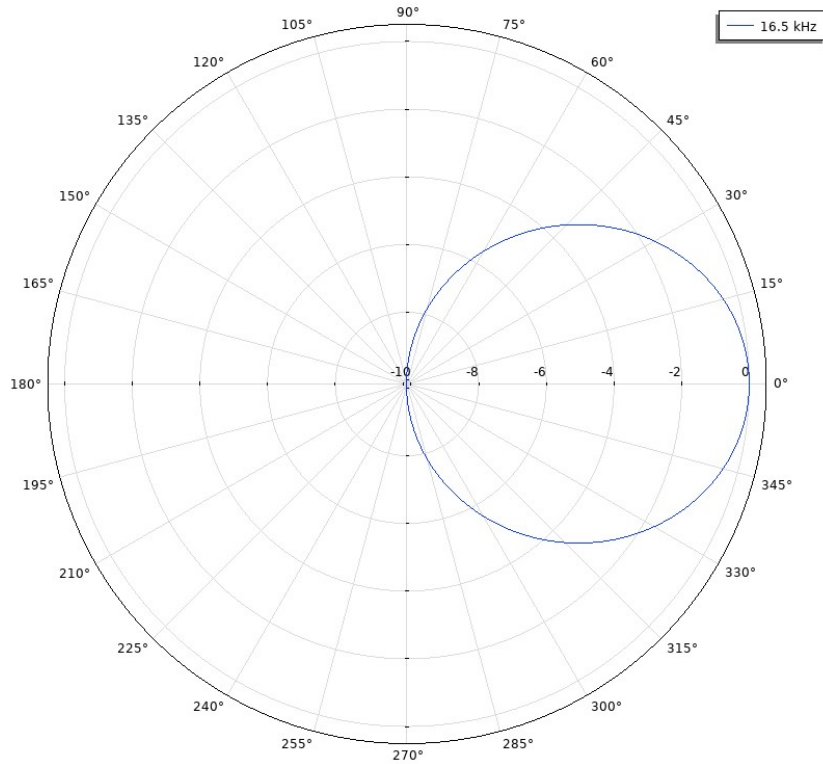
Figure 21. Beam pattern of a single-element Tonpilz transducer

3.4 Array Simulations

As previously mentioned, arrays are typically employed to achieve optimal acoustic performance. The performance of arrays depends on several factors: the number of constituent elements, their spacing, operating frequency, and array geometry. This section presents simulation results for several planar arrays with square, circular, and diamond configurations. The input electrical impedance, transmitted voltage response, and beam patterns of these arrays are analyzed and compared. A 1 Volt RMS alternating voltage was applied to each transducer. The array simulations were conducted in COMSOL Multiphysics software using the boundary element method.

3.5 The Effect of Element Spacing on the Performance of a Square Array

Figures 22 and 23 demonstrate the effect of element spacing variations on the input electrical impedance and transmitted voltage response of a 3×3 square array. The red, blue, and black curves, respectively, represent transducer spacings of $0.5\lambda, 0.4\lambda$, and 0.6λ, where λ denotes the wavelength.
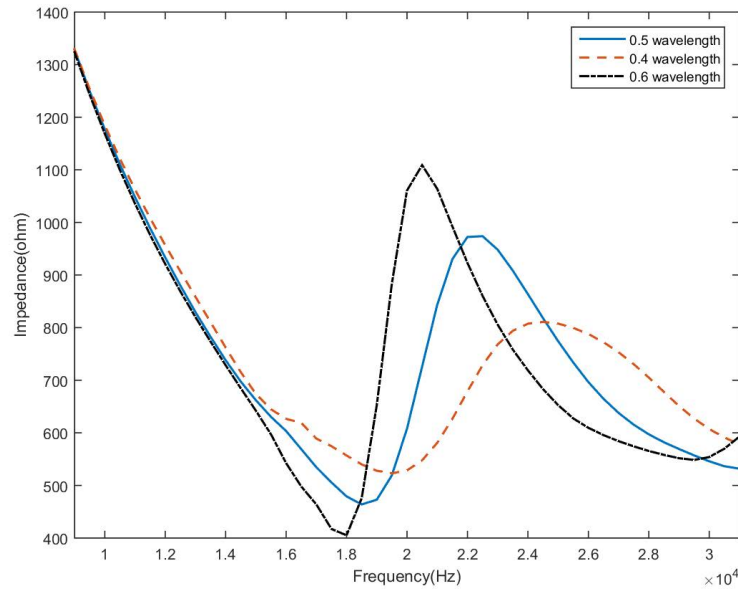
**Figure 22.** Comparison of electrical impedance curves for three square arrays
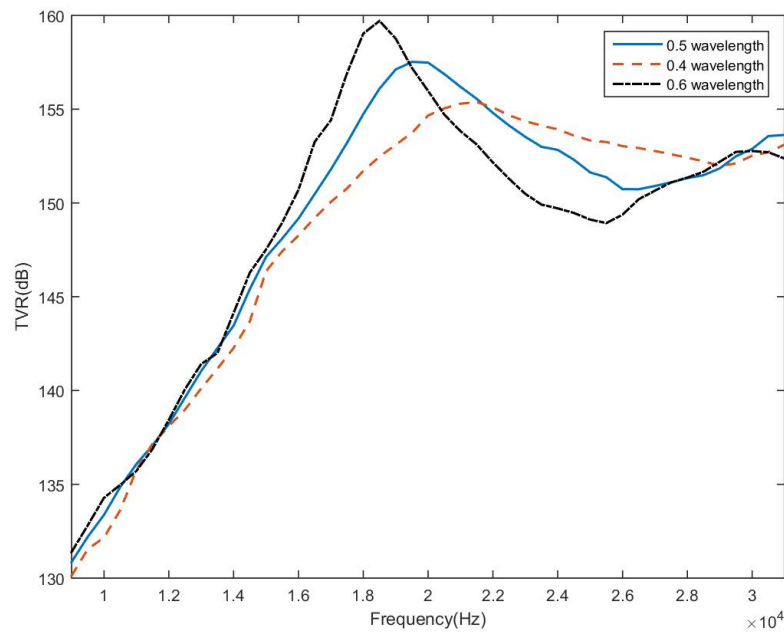
**Figure 23.** Comparison of transmitted voltage response (TVR) curves for three square arrays

As can be seen in Table 3, the obtained resonance frequency values from the transmitted voltage response diagrams show slight differences compared to those obtained from the input electrical impedance plots. After calculating the maximum transmitted voltage response of the arrays, the bandwidth and quality factor for each array can be determined by drawing a horizontal line parallel to the x-axis that passes through this maximum value.

Table 3. Impact of inter-element distance on resonance frequency, bandwidth, and quality factor in square arrays

Square Arrays	The Distance Between Elements	Resonance Frequency	Antiresonance Frequency	Resonance Frequency (TVR)	Transmitter Operating Bandwidth	Receiver Operating Bandwidth	Quality Factor	Beam Bandwidth
1	0.5λ	18.5	22.5	19.5	4.3	4.5	4.30	28.6
2	0.4λ	19.5	24.5	21.5	9.6	8	8	38.1
3	0.6λ	18	20.5	18.5	2.2	18.5	2.8	29.5

According to Table 3, the square array with an inter-element spacing of 0.4λ exhibits the widest bandwidth. A larger array bandwidth directly correlates with a broader operational range. Table 3 further reveals that the second and third arrays demonstrate the lowest and highest quality factors, respectively. The quality factor serves as a metric for evaluating both frequency sharpness and array efficiency. Arrays with higher quality factors show greater efficiency and sharper resonance frequencies. The superior efficiency of the third array is also evident in Figure 23, where it displays the highest transmitted voltage response at its resonance frequency compared to the other two arrays.
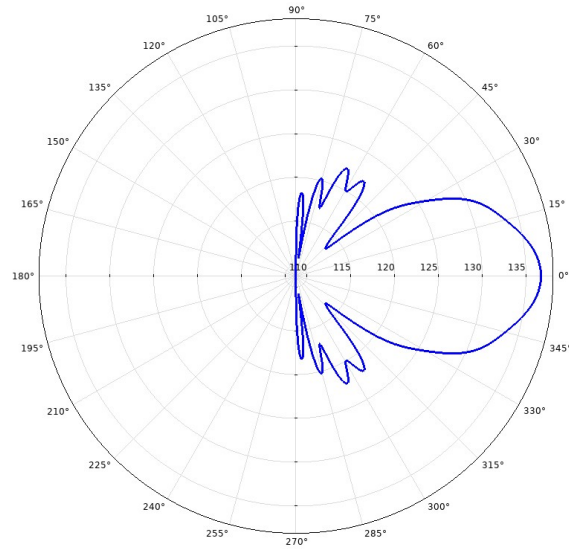

Figure 24. Beam pattern of square array with inter-element spacing of 0.5λ
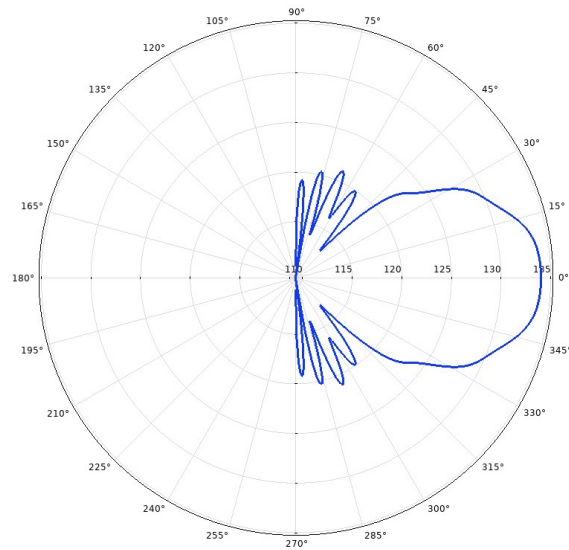
Figure 25. Beam pattern of square array with inter-element spacing of 0.4λ
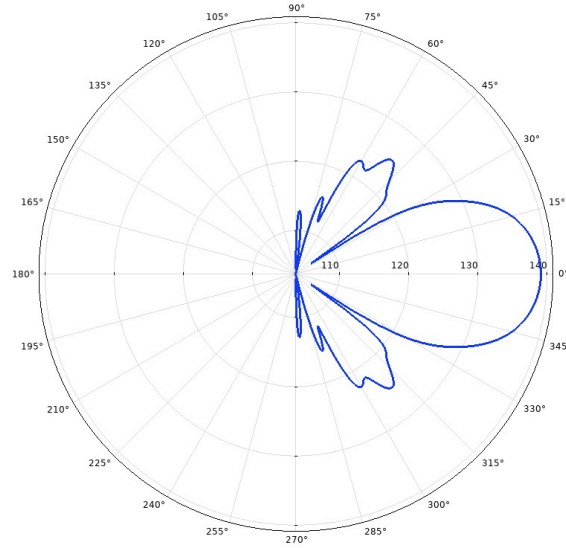
Figure 26. Beam pattern of square array with inter-element spacing of 0.6λ

The simulated square arrays in this study are positioned in the xy-plane. Figures 24 through 26 present the beam patterns of these arrays at their resonance frequencies in both xz and yz planes (the planes perpendicular to the array surface and intersecting its edges). Due to the array's symmetrical geometry, the beam patterns are identical in these planes. As shown in Table 3, the second array has the broadest beamwidth while the first array shows the narrowest. A smaller beamwidth indicates a more focused beam pattern, meaning most of the array's emitted energy concentrates along a specific direction. This characteristic enhances target localization in sonar systems. Conversely, a larger beamwidth provides a wider field of view.

As shown in Figures 24 to 26, the side lobe levels in the first and second arrays are approximately equal, but reach their maximum value in the third array. The presence of side lobes in transmission mode indicates that the array radiates signals in directions other than the main beam direction. These side lobes lead to increased interference, reduced signal-to-noise ratio, and decreased accuracy in target detection. Overall, side lobes reduce both the main lobe's energy and the array's sensitivity to weaker signals, and should be minimized whenever possible.
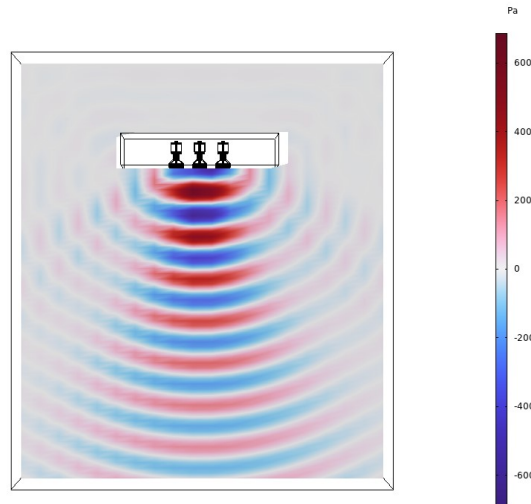
**Figure 27.** Acoustic pressure distribution plot of the square array

Figure 27 shows the acoustic pressure distribution for a square array when the distance between elements equals half the wavelength. As previously explained, the array elements vibrate when an alternating voltage is applied, converting electrical energy into mechanical energy. These vibrations create pressure waves that generate acoustic pressure. The total acoustic pressure of the array is defined as the sum of the acoustic pressures produced by each constituent element. Typically, the array structure is designed and the input electrical signals are optimized such

that the vibrations of the transducers forming the array become phase-synchronized in a specific desired direction, producing a strong acoustic field.

When the array generates acoustic waves, it creates regions of high pressure and low pressure in the medium. The high-pressure region is where water or air particles are compressed closer together, while the low-pressure region is where these particles are more dispersed. These regions are represented by red and blue colors respectively in Figure 27. As shown, the total acoustic pressure is positive in the red regions and negative in the blue regions. This indicates that the vibrations of the transducers comprising the array are in-phase in the red regions, resulting in constructive interference. Consequently, environmental pressure increases in these areas, producing positive pressure variations. Conversely, the transducer vibrations are out-of-phase in the blue regions, causing destructive interference. This leads to reduced environmental pressure and negative pressure variations in these areas.

3.6 The Effect of the Number of Elements on the Performance of a Circular Array

Figures 28 and 29 demonstrate the effect of increasing the number of elements in a circular array on both the input electrical impedance diagrams and the transmitted voltage response. The first array consists of 8 transducers, while the second array comprises 12 transducers. In both arrays, the inter-element spacing is set at half-wavelength distance. As evident in the input electrical impedance diagram, the array composed of 12 elements exhibits lower resistance to the input electrical signal, consequently resulting in higher electrical efficiency and greater acoustic output. This observation is further corroborated by the transmitted voltage response (TVR) plots of the arrays, where the larger array demonstrates a higher TVR magnitude compared to the smaller array.
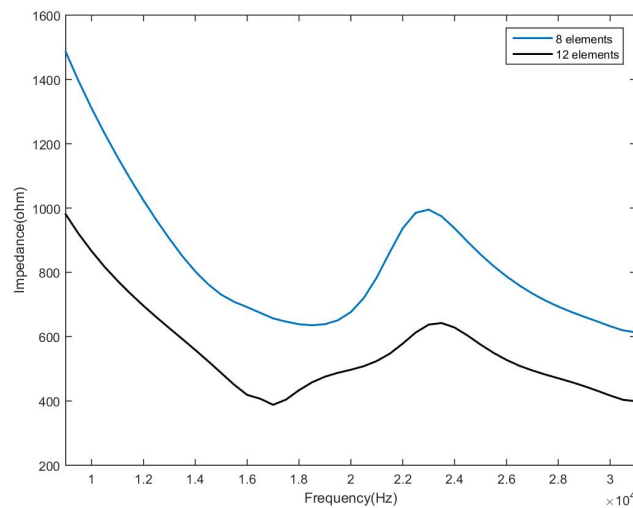
**Figure 28.** Effect of the number of elements on array input electrical impedance
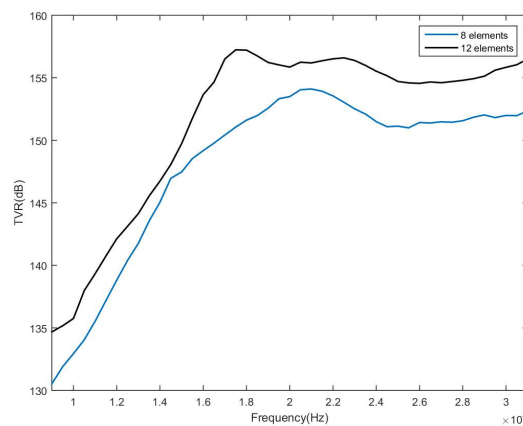
Figure 29. Effect of the number of elements on transmit voltage response (TVR)

Table 4. Impact of inter-element distance on resonance frequency, bandwidth, and quality factor in square arrays

The Number of Elements	Resonance Frequency	Antiresonance Frequency	Resonance Frequency (TVR)	Transmitter Array Bandwidth	Quality Factor	Beam Bandwidth
8	18.5	23	21	8.1	2.28	27.2
12	17	23.5	17.5	9.7	9.7	20.3

As shown in Figure 29, increasing the number of elements leads to a wider bandwidth. Table 4 presents the simulated resonance frequency, bandwidth, quality factor, and beamwidth values for the two circular arrays. The beam patterns of these two arrays are shown in Figures 30 and 31. As can be observed, the circular array composed of 12 elements exhibits a narrower beamwidth with slimmer side lobes. The reduced side lobe width indicates this array's superior directivity. Further reduction of side lobe levels can be achieved by decreasing the inter-element spacing. Figure 32 displays the sound pressure level (SPL) contour plot for the circular array consisting of 8 elements. As previously mentioned, this plot represents the sound intensity or acoustic energy distribution in space. The beam pattern of the array is clearly visible in this plot, with red regions indicating the highest sound intensity and blue regions showing the lowest intensity.
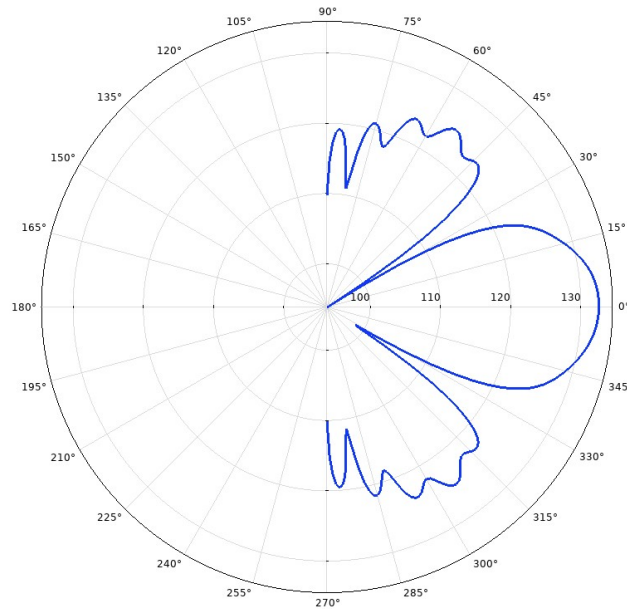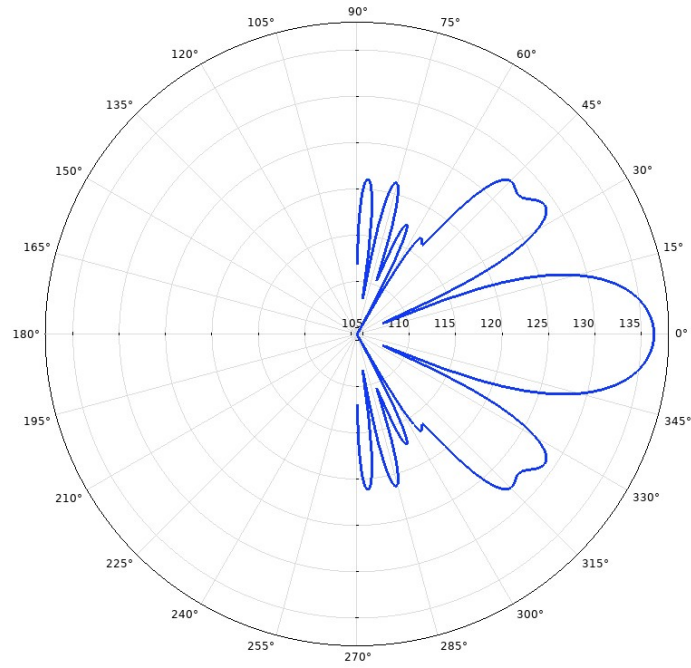

Figure 30. Beam pattern of circular array composed of 8 elements

### 3.7 The Impact of Structural Modifications on Array Performance

When a square array with inter-element spacing equal to half the wavelength is rotated by 45 degrees, a diamond-shaped array is formed. In this configuration, the actual distance between elements is effectively reduced. Consequently, the input electrical impedance and transmitted voltage response remain identical to those of the square array, and the beamwidth shows negligible change compared to the square array (27.6 degrees). However, the side lobes become smaller. The resulting beam pattern in this case is identical to the beam pattern of the square array in the plane perpendicular to the array surface and passing through its diagonal. Figure 33 illustrates the beam pattern of the diamond-shaped array.

Table 5. Impact of structural changes on resonance frequency, bandwidth, and quality factor

| Array Configuration	Resonance Frequency	Ntiresonance Frequency	Resonance Frequency (TVR)	Bandwidth	Quality Factor	Beam Bandwidth (xz)	Beam Bandwidth (yz)
Circular	17	23.5	17.5	9.7	1.75	20.3	20.3
Square	18.5	22.5	19.5	4.1	4.51	28.8	22

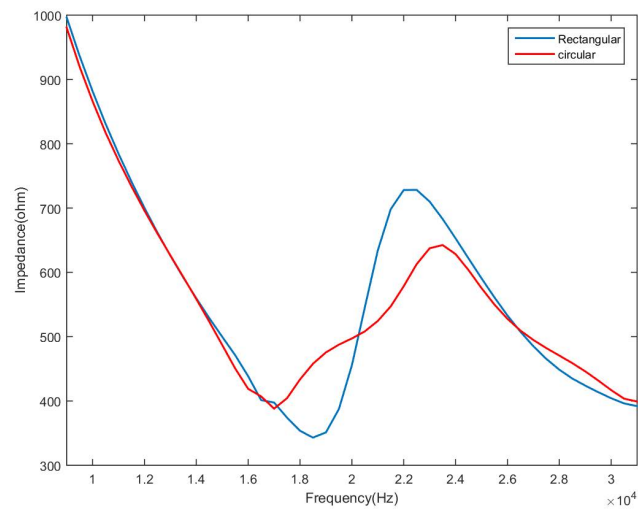**Figure 31.** Beam pattern of circular array composed of 12 elements
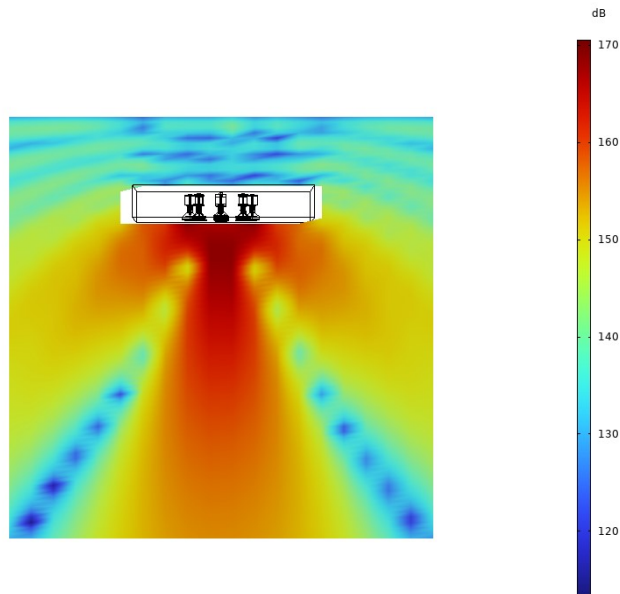
**Figure 32.** Sound pressure level (SPL) contour plot for the circular array of 8 elements

Figures 34 and 35 display the input electrical impedance and transmitted voltage responses of two arrays composed of 12 elements. The red curve corresponds to the circular array configuration, while the blue curve represents the square array. In both types, the inter-element spacing is set at half-wavelength distance. As observed, the circular array exhibits a wider bandwidth compared to the square array. Figure 36 illustrates the beam pattern of the square array in two planes perpendicular to the array surface, each passing through one pair of its sides. The blue curve corresponds to the plane passing through the longer side of the array, while the green curve represents the plane passing through the shorter side. Table 5 presents the resonance frequency, anti-resonance frequency, bandwidth, and quality factor values for both circular and square arrays.
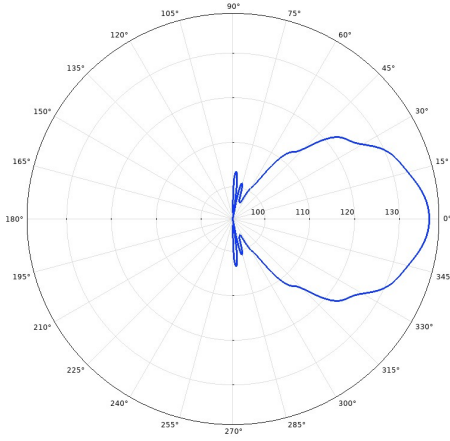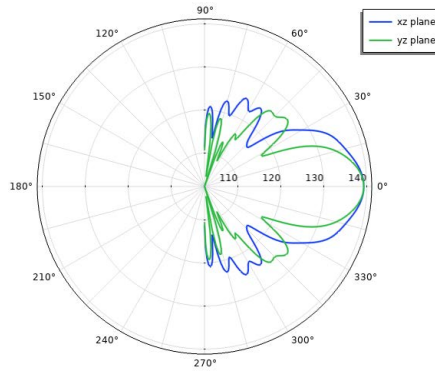
Figure 33. Beam pattern of the diamond-shaped array with 0.5λ inter-element spacing

Figure 34. Comparison of input electrical impedance for circular and square arrays
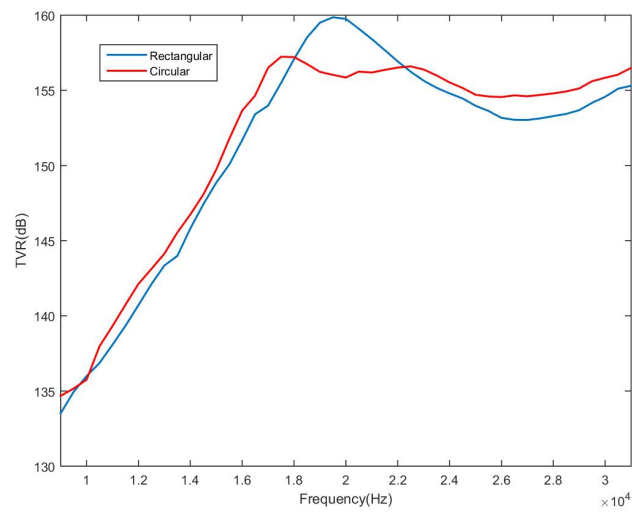
Figure 35. Comparison of transmitted voltage responses for circular and square arrays

Figure 36. Beam pattern of square array

4 Conclusions

The aim of this research was to identify and estimate the bandwidth of ultrasonic arrays and predict their performance using numerical methods. In this regard, the frequency-domain behavior of a Tonpilz transducer was first investigated using MATLAB and COMSOL software. Subsequently, several planar arrays with square, circular, and diamond configurations were simulated, and the effects of inter-element spacing, number of elements, and array configuration on input electrical impedance, transmitted voltage response, and beam patterns were examined. Following analysis and comparison of the findings of this study, the following results were obtained:

- The Mancic matrix model can appropriately predict the first thickness mode and first radial mode of a piezoceramic ring. Since these two modes have the most industrial applications, this model can serve as a simple tool for transducer design and optimization.

- At resonance frequency, the tail mass exhibits minimal displacement while the head mass shows maximum displacement. Consequently, the transducer demonstrates optimal performance at this frequency.

- The beam width of the Tonpilz transducer used in this study measures 82.5° at its resonance frequency. To reduce this value, an array of transducers should be employed instead of a single transducer.

- Among three square arrays with different inter-element spacing, the array with 0.4λ spacing between constituent transducers demonstrates the widest bandwidth. This indicates superior image resolution and accuracy in transmission mode compared to the other two arrays.

- Among three kinds of square arrays, the array with 0.6λ spacing shows the highest quality factor, meaning it has greater efficiency, sharper resonance frequency, and narrower bandwidth than the other arrays.

- The array with 0.4λ spacing produces the widest beam pattern among the three kinds of square arrays, resulting in more focused directivity and greater beam directionality.

- The input electrical impedance and transmitted voltage response diagrams of the diamond-shaped array closely resemble those of the square array, with minimal change in beam width. However, its side lobes are smaller. Since side lobes reduce the main lobe's energy and array sensitivity to weaker signals, they should be minimized when possible.

- The circular array exhibits wider bandwidth than the square array while maintaining a narrower beam width.

References

[1] M. J. Sim, W. B. Jeong, and C. Hong, "An equivalent circuit based electrovibro-acoustic model of a cylindrical transducer array," *J. Acoust. Soc. Am.*, vol. 149, no. 5, pp. 3228–3240, 2021. https://doi.org/10.1121/10.0004952

[2] M. O. Saçma, "Mutual impedance considerations in two dimensional planar acoustic arrays with square piston elements," Master's thesis, Bilkent Univ. (Turkey), 2015.

[3] M. D. Randmanovič and D. D. Mančič, *Design and Modeling of the Power Ultrasonic*. Niš: Faculty of Electronic Engineering, 2004.

[4] C. H. Sherman and J. L. Butler, *Transducers and Arrays for Underwater Sound*. New York, NY: Springer, 2007. https://doi.org/10.1007/978-0-387-33139-3

[5] N. M. Nouri, H. R. Gharavian, and A. Valipour, "Simulation and optimization of tonpilz transducer by FEM and comparing the results with electroacoustic tests," *Modares Mech. Eng.*, vol. 14, pp. 63–70, 2014.

[6] "Ultrasonic advisors," https://www.ultrasonicadvisors.com/, visited on 2023-09-20.

[7] X. Meng and S. Lin, "Analysis on coupled vibration of piezoelectric ceramic stack with two piezoelectric ceramic elements," *J. Acoust. Soc. Am.*, vol. 146, no. 4, pp. 2170–2178, 2019. https://doi.org/10.1121/1.5126866

[8] X. Meng and S. Lin, "Analysis of a cascaded piezoelectric ultrasonic transducer with three sets of piezoelectric ceramic stacks," *Sensors*, vol. 19, no. 3, p. 580, 2019. https://doi.org/10.3390/s19030580

[9] A. Ballato, "Modeling piezoelectric and piezomagnetic devices and structures via equivalent networks," *IEEE Trans. Ultrason. Ferroelectr. Freq. Control*, vol. 48, no. 5, pp. 1189–1240, 2001. https://doi.org/10.1109/58.949732

[10] A. Iula, N. Lamberti, and M. Pappalardo, "A model for the theoretical characterization of thin piezoceramic rings," *IEEE Trans. Ultrason. Ferroelectr. Freq. Control*, vol. 43, no. 3, pp. 370–375, 1996. https://doi.org/10.1109/58.489393

[11] A. Iula, N. Lamberti, and M. Pappalardo, "An approximated 3-D model of cylinder-shaped piezoceramic elements for transducer design," *IEEE Trans. Ultrason. Ferroelectr. Freq. Control*, vol. 45, no. 4, pp. 1056–1064, 1998. https://doi.org/10.1109/58.710588

[12] D. D. Mančić and M. D. Radmanović, "Piezoceramic ring loaded on each face: A three-dimensional approach," *Electron. J. Tech. Acoust.*, vol. 2, pp. 1–7, 2002.

[13] H. Jalili and H. Goudarzi, "Modeling the hollow cylindrical piezo-ceramics with axial polarization using equivalent electro-mechanical admittance matrix," *Sens. Actuators A Phys.*, vol. 149, no. 2, pp. 266–276, 2009. https://doi.org/10.1016/j.sna.2008.11.016

[14] D. D. Mančić and G. Z. Stančić, "New three-dimensional matrix models of the ultrasonic sandwich transducers," *J. Sandw. Struct. Mater.*, vol. 12, no. 1, pp. 63–80, 2010.

[15] H. Kim and Y. Roh, "Design and fabrication of a wideband Tonpilz transducer with a void head mass," *Sens. Actuators A Phys.*, vol. 239, pp. 137–143, 2016. https://doi.org/10.1016/j.sna.2016.01.029

[16] H. C. Harikrishnan, K. Kiran, and A. Malarkodi, "Finite element analysis of underwater acoustic vector sensor," *IEEE Underwater Technol. (UT)*, no. 1, pp. 1–4, 2015. https://doi.org/10.1109/UT.2015.7108301

[17] Y. Gou, S. Ye, X. Fu, F. Zheng, X. Zha, and C. Li, "Optimizing Tonpilz transducer transmission through impedance matching and head mass structure," *Micromachines*, vol. 16, no. 3, p. 352, 2025. https://doi.org/10.3390/mi16030352

[18] X. Ji, T. Yang, and D. Wang, "Experimental investigation of a Tonpilz transducer using non-uniform piezoceramic stacks," *J. Acoust. Soc. Am.*, vol. 155, no. 6, pp. 3600–3611, 2024.

[19] M. Hadeed, H. S. Bhatti, M. S. Afzal, V. Epin, and M. Abdullah, "Design and development of a high-power wideband multimode Tonpilz transducer for underwater applications," *J. Mech. Eng. Sci.*, vol. 18, no. 3, pp. 10 161–10 170, 2024. https://doi.org/10.15282/jmes.18.3.2024.5.0802

[20] S. Pyo, M. S. Afzal, Y. Lim, S. Lee, and Y. Roh, "Design of a wideband tonpilz transducer comprising non-uniform piezoceramic stacks with equivalent circuits," *Sensors*, vol. 21, no. 8, p. 2680, 2021. https://doi.org/10.3390/s21082680

[21] F. Karami and R. Morsali, "Optimization of sonar transducers via evolutionary algorithms," *SN Appl. Sci.*, vol. 1, p. 1728, 2019. https://doi.org/10.1007/s42452-019-1803-7

[22] A. V. Pigatto, L. Giacobbo, A. Lisibach, E. M. Lopes Filho, R. G. Lima, and J. L. Mueller, "Design and calibration of a tonpilz transducer for low frequency medical ultrasound tomography," in *2022 44th Annual International Conference of the IEEE Engineering in Medicine & Biology Society (EMBC)*, Glasgow, Scotland, United Kingdom, 2022. https://doi.org/10.1109/EMBC48229.2022.9872007

[23] J. Chen, C. Gong, G. Yue, L. Zhang, X. Wang, Z. Huo, and Z. Dong, "Structural optimization and performance of a low-frequency double-shell type-IV flexural hydroacoustic transducer," *Sensors*, vol. 24, no. 14, p. 4746, 2024. https://doi.org/10.3390/s24144746

[24] I. Jovanović, D. Mančić, V. Paunović, M. Radmanović, and Z. Petrušić, "A Matlab / Simulink model of piezoceramic ring for transducer design," *A A*, vol. 11, no. 12, p. 13, 2011.

[25] M. Brissaud, "Characterization of piezoceramics," *IEEE Trans. Ultrason. Ferroelectr. Freq. Control*, vol. 38, no. 6, pp. 603–617, 1991. https://doi.org/10.1109/58.108859

[26] G. Hayward and D. Gillies, "Block diagram modeling of tall, thin parallelepiped piezoelectric structures," *J. Acoust. Soc. Am.*, vol. 86, no. 5, pp. 1643–1653, 1989. https://doi.org/10.1121/1.398594

[27] I. Jovanovic, D. Mancic, V. Paunovic, M. Radmanovic, and V. V. Mitic, "Metal rings and discs Matlab/Simulink 3D model for ultrasonic sandwich transducer design," *Sci. Sinter.*, vol. 44, no. 3, pp. 287–298, 2012. https://doi.org/10.2298/SOS1203287J

[28] K. Çepni, "A methodology for designing tonpilz-type transducers," Ph.D. dissertation, Middle East Tech. Univ., 2011.

[29] I. Jovanovic, U. Jovanovic, and D. Mancic, "A Matlab/Simulink 3D model of unsymmetrical ultrasonic sandwich transducers," *Serb. J. Electr. Eng.*, vol. 15, no. 1, pp. 41–52, 2018. https://doi.org/10.2298/SJEE1801041J

[30] S. H. H. Kachapi and S. G. H. Kachabi, "Nonclassical and nonlinear stability analysis of viscous fluidic

piezoelectric biomedical nanosensor," *Spectr. Mech. Eng. Oper. Res.*, vol. 2, no. 1, pp. 59–77, 2025. https://doi.org/10.31181/smeor21202530

[31] R. Tantawy and A. Zenkour, "Even and uneven porosities on rotating functionally graded variable-thickness annular disks with magneto-electro-thermo-mechanical loadings," *J. Appl. Comput. Mech.*, vol. 9, no. 3, pp. 695–711, 2023. https://doi.org/10.22055/jacm.2022.42114.3875

[32] Ž. Ćojbašić, N. Ivačko, D. Marinković, P. Milić, G. Petrović, M. Milošević, and N. Marković, "Isogeometric finite element analysis with machine learning integration for piezoelectric laminated shells," *J. Eng. Manag. Syst. Eng.*, vol. 2, no. 4, pp. 196–203, 2023. https://doi.org/10.56578/jemse020401

[33] E. Noh, H. Lee, W. Chun, W. S. Ohm, K. Been, W. Moon, and H. Yoon, "Iterative solutions of the array equations for rapid design and analysis of large projector arrays," *J. Acoust. Soc. Am.*, vol. 144, no. 4, pp. 2434–2446, 2018. https://doi.org/10.1121/1.5065493

[34] S. Pyo, Y. Lim, and Y. Roh, "Analysis of the transmitting characteristics of an acoustic conformal array of multimode tonpilz transducers by the equivalent circuit method," *Sens. Actuators A Phys.*, vol. 318, p. 112507, 2021. https://doi.org/10.1016/j.sna.2020.112507

[35] M. A. Heidari and M. M. Abootorabi, "Design and simulation of an array consisted of Tonpilz transducers with protective coating materials," *Iran. J. Manuf. Eng.*, vol. 2, pp. 11–19, 2016.